PERGAMON

International Journal of Heat and Mass Transfer 41 (1998) 3899–3918

International Journal of HEAT and MASS TRANSFER

# Pulsative heating of surfaces

S. Z. Shuja*, B. S. Yilbas

*Department of Mechanical Engineering, King Fahd University of Petroleum and Minerals, Dhahran 31261, Saudi Arabia*

Received 5 November 1997; in final form 17 February 1998

**Abstract**

Laser repetitive pulse heating is one of the research fields in laser heating of engineering surfaces. The effect of assisting gas jet on the laser heating process is usually omitted in the previous studies. The present study examines the gas jet assisted laser repetitive pulse heating of steel surfaces. The flow and temperature fields are predicted numerically using the control volume approach. The two-dimensional axisymmetric heat conduction equation is solved for the solid substance, while continuity, momentum, energy and equation of state are considered for the impinging air, which is introduced coaxially with the laser beam and orthogonal to the workpiece surface as the assisting gas. The low Reynolds number $k$–$\varepsilon$ model is used to account for the turbulence in the flow field. The solid and gas properties are considered as variable. The study is extended to include three pulse types and two gas jet velocities. It is found that the thermal integration for the repetitive pulses of high cooling periods is unlikely and the effect of gas jet velocity is not substantial on the resulting solid side temperature profiles. 

**Nomenclature**

$a$ constant in Gaussian function
$b$ constant in equation (10)
$c_p$ specific heat capacity
$C_1$, $C_2$, $C_\mu$ coefficient in the $k$–$\varepsilon$ turbulence model
$D$ diameter of the nozzle (1 mm)
$f_1$, $f_2$, $f_\mu$ coefficient in the low Reynolds number, $k$–$\varepsilon$ model
$f(t)$ time variation of pulse shape
$G$ rate of generation of $k$
$I_0$ peak power intensity
$k$ turbulent kinetic energy
$K$ thermal conductivity
$p$ pressure
$r$ distance in the radial direction
$Re$ Reynolds number
$S$ unsteady spatially varying source defined in equation (13)
$S_\phi$ source term for variable $\phi$
$t$ time
$T$ temperature
$\bar{u}$ average inlet velocity
$u^*$ wall-friction velocity
$U$ arbitrary velocity
$V$ radial velocity
$W$ axial velocity
$x$ arbitrary direction
$z_n$ distance to the nearest wall
$z$ distance in the axial direction
$z^+$ dimensionless axial distance $= \rho z u^*/\mu$.

*Greek symbols*

$\delta$ absorption coefficient
$\varepsilon$ energy dissipation
$\lambda$ a fraction of $\bar{u}$ typically 0.03
$\mu$ variable dynamic viscosity (function of temperature for laminar)
$\nu$ variable kinematic viscosity (function of temperature for laminar)
$\rho$ density (function of temperature and pressure for gas)
$\sigma$ variable Prandtl number (function of temperature)
$\phi$ arbitrary variable
$\Phi$ viscous dissipation.

*Subscripts*

amb ambient
e effective, e.g. $\mu_e = u + u_t$
$i, j$ arbitrary direction

* Corresponding author. Tel.: 00966 3 8606458; fax: 00966 3 8602949; e-mail shuja@ccse.kfupm.edu.sa

0017–9310/98 $19.00 
PII: S0017–9310(98)00078–7

l laminar
t turbulent
w wall.

## 1. Introduction

The use of lasers in industry has initiated the development of several model calculations of both spatial and temporal temperature profiles in laser heated solids. Analytical and numerical solution have been proposed for treating the ensuing heat flow under a variety of simplifying assumptions and approximations. However, they are part of a continuous effort to produce reliable predictions of those temperature distributions which are of capital importance for in-depth analysis and improvement of the processes. The practical applications of high power lasers are machining, welding and surface treatment of engineering parts. The surface treatment application of lasers depends on the laser's ability to produce structures which may not be possible with conventional methods, relying on such laser attributes as narrow heat-affected zone, treatment of inaccessible locations, precision of operation and low cost of operation.

Heat transfer mechanisms initiating the laser heating of surfaces have been carried out by many researchers [1–3]. Their studies were limited to solid or liquid phase heating; in which case, the influence of assisting gas jet on the process was neglected. Osawa et al. [4] studied the effect of laser heat treatment on intergranular corrosion of austenitic stainless steel, while thermal analysis for laser surface hardening of steel was conducted by Toyal and Mukherjee [5]. The closed form solution for conduction limited laser heating was accomplished by Yilbas [6]. He indicated that the thermal integration of the pulsed heating was possible for the pulse repetition rate of about 1 kHz. However, the analysis was limited to one dimensional and the assisting gas effect during the heating operation was omitted. The laser heating of the surfaces, is, in general, a gas assisted process; in which case, the function of this assisting gas is either to protect the surface against the oxidizing environment or to cool down the surface for improved hardness [7]. Consequently, when modeling the repetitive pulse laser heating of the engineering surfaces, assisted gas effect should be considered. The turbulent assisting gas jet impinging orthogonally onto a plane surface produces a stagnation point flow. The overall heat-or mass-transfer performance of jet impingement configuration has been examined by a considerable number of researchers [8, 9]. Analytical solutions for the flame impingement heat transfer were reviewed by Baukal and Gebhart [10] while an alternative formulation for the stagnation point flow was carried out by Abid and Speziale [11]. They used the standard $k$–$\varepsilon$ model to account for the turbulence in stagnation point flow. They indicated that the solution was not visible and vortex stretching effects in the turbulent dissipation rate equation should be considered. Strahle et al. [12] introduced two equation models for variable density stagnation point flow. They concluded that the two equation models were applicable for low Reynolds number flows.

In order to investigate the effect of gas impingement on the laser heating process, the present study is conducted in which the two-dimensional axisymmetric repetitive pulse laser heating of a steel surface is considered. Air is introduced as an assisting gas impinging coaxially with the laser beam and orthogonal to the workpiece surface. The transient two-dimensional axisymmetric heat transfer equation is solved numerically to compute the temperature profiles in the solid while continuity, momentum, energy and equation of state are considered to predict the flow field in the gas side. Low Reynolds number $k$–$\varepsilon$ model is introduced to account for the turbulence. The solid and gas properties are considered as variable to simulate the process more realistically. The study is extended to include two gas jet velocities and three repetitive pulse types.

## 2. The mathematical model

### 2.1. *Flow equations in physical space*

Figure 1(a) shows the schematic view of the nozzle and the workpiece. To predict the flow field due to jet impingement, it is necessary to solve the unsteady two-dimensional axisymmetric form of the continuity and the time-averaged Navier–Stokes equations. In the Cartesian Tensor system, the continuity and momentum equations are:

$$\frac{\partial \rho}{\partial t} + \frac{\partial}{\partial x_i}(\rho U_i) = 0 \tag{1}$$

and

$$\frac{\partial}{\partial t}(\rho U_j) + \frac{\partial}{\partial x_i}(\rho U_i U_j) = -\frac{\partial p}{\partial x_j} + \frac{\partial}{\partial x_i}\left[(\mu_t + \mu)\frac{\partial U_j}{\partial x_i}\right] \tag{2}$$

where $\mu_t$, is the eddy viscosity, which has to be specified by a turbulence model. The partial differential equation governing the transport of thermal energy has the form:

$$\frac{\partial T}{\partial t} + \frac{\partial}{\partial x_i}(U_i T) = \frac{\partial}{\partial x_i}\left[\left(\frac{\mu_t}{\sigma_t} + \frac{\mu}{\sigma}\right)\frac{\partial T}{\partial x_i}\right]. \tag{3}$$

Turbulence equations:

The turbulent viscosity, $\mu_t$, can be defined using the two-equation $k$–$\varepsilon$ model of turbulence [13], i.e.:

$$\mu_t = C_\mu \rho k^2/\varepsilon \tag{4}$$

where $C_\mu$ is an empirical constant and $k$ is the turbulence kinetic energy which is given by

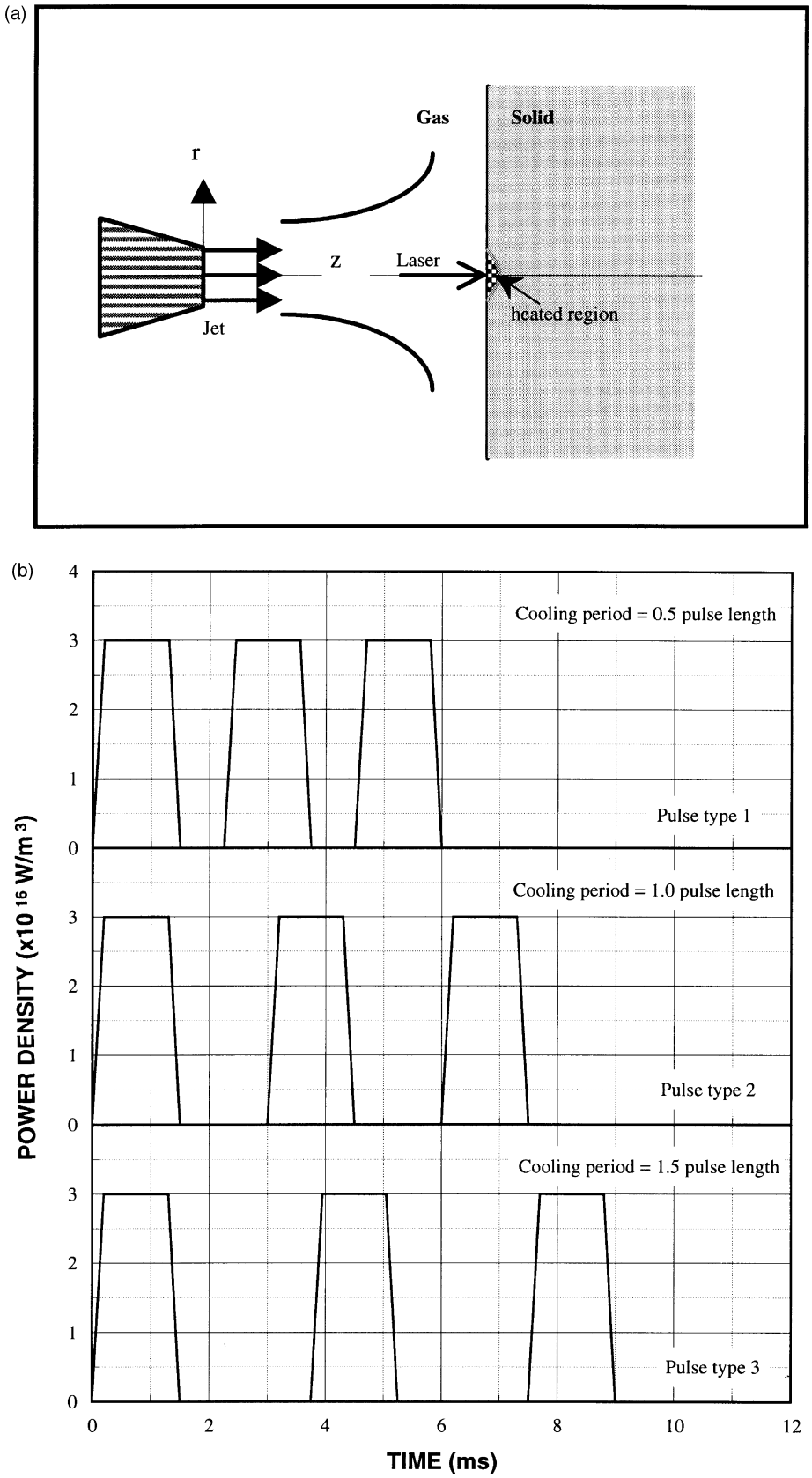


Fig. 1(a). Schematic view of gas jet impingement onto laser heated spot. (b) Successive pulses used in the analysis.

$$\frac{\partial}{\partial t}(\rho k)+\frac{\partial}{\partial x_i}(\rho U_i k)=\frac{\partial}{\partial x_i}\left[\left(\frac{\mu_t}{\sigma_k}+\mu\right)\frac{\partial k}{\partial x_i}\right]+G-\rho\varepsilon \quad (5)$$

similarly $\varepsilon$ is the energy dissipation which is given by the following differential equation

$$\frac{\partial}{\partial t}(\rho\varepsilon)+\frac{\partial}{\partial x_i}(\rho U_i\varepsilon)=\frac{\partial}{\partial x_i}\left[\left(\frac{\mu_t}{\sigma_\varepsilon}+\mu\right)\frac{\partial \varepsilon}{\partial x_i}\right]+\frac{\varepsilon}{k}(C_1G-C_2\rho\varepsilon) \quad (6)$$

$G$ represents the rate of generation of turbulent kinetic energy and $\rho\varepsilon$ is its destruction rate. $G$ is given by

$$G=\mu_t\left[\left(\frac{\partial U_i}{\partial x_j}+\frac{\partial U_j}{\partial x_i}\right)\frac{\partial U_i}{\partial x_j}\right]. \quad (7)$$

The model contains six empirical constants which are assigned the following values:

| $C_\mu$ | $C_1$ | $C_2$ | $\sigma_k$ | $\sigma_\varepsilon$ |
|---|---|---|---|---|
| 0.09 | 1.44 | 1.92 | 1.00 | 1.00 |

The $k$–$\varepsilon$ model is only applicable in the regions where the flow is entirely turbulent, and close to the solid walls viscous effects become dominant; in this case, such a model does not lead to acceptable predictions. Consequently, corrections in the $k$–$\varepsilon$ may be needed. In the light of the previous study [12], the low Reynolds number $k$–$\varepsilon$ model is considered to account for the turbulence. The Lam–Bremhorst low-Reynolds number extension to the $k$–$\varepsilon$ model employs a transport equation for the total dissipation rate [14]. It differs from the standard high-Reynolds number model in that the empirical coefficients $C_\mu$, $C_1$ and $C_2$ are multiplied, respectively, by the functions:

$$f_\mu=(1-e^{-0.0165Re_l})^2\left(1+\frac{20.5}{Re_t}\right)$$

$$f_1=1+\left(\frac{0.05}{f_\mu}\right)^3$$

$$f_2=1-e^{-Re_t^2}$$

where $Re_l=z_n\sqrt{k}/\nu_l$ and $Re_t=k^2/\varepsilon\nu_l$; and $z_n$ is the distance to the nearest wall. For high-turbulence Reynolds numbers, $Re_l$ or $Re_t$, the functions $f_\mu$, $f_1$ and $f_2$ multiplying the three constants tend to unity.

### 2.2. Boundary conditions for low-Reynolds number model

Laminar boundary conditions are set for the mean-flow variables, and the boundary conditions $k=0$ and $(d\varepsilon/dz)=0$ are applied at the wall. Since the low-Reynolds number extension does not employ wall functions, and the flow field needs to be meshed into the laminar sublayer and down to the wall, the computer storage and run-time requirements for this approach are much greater than those of the wall-function approach. In general the grid employed normal to the main direction needs to be distributed so as to give a high concentration of grid cells near the wall, with the wall-adjacent node positioned at $z^+=(\rho zu^*/\mu)=1.0$ or even less.

Inlet conditions:

$$U_i=\text{specified} \quad \text{and} \quad T=\text{constant}. \quad (8)$$

Values of $k$ and $\varepsilon$ are not known at the inlet but, some reasonable assumptions can be made. The kinetic energy of turbulence is estimated according to some fraction of the square of the average inlet velocity:

$$k=\lambda\bar{u}^2 \quad (9)$$

where $\bar{u}$ is the average inlet velocity and $\lambda$ is a fraction.

The dissipation is calculated according to the equation

$$\varepsilon=C_\mu\frac{k^{3/2}}{bD} \quad (10)$$

where $D$ is the inlet diameter. The values $\lambda=0.03$ and $b=0.005$ are commonly used and may vary slightly in the literature [15].

Outlet:

It is considered that the flow extends over a sufficiently long domain so that it is fully developed at the exit section. Thus for any variable $\phi$ the condition is

$$\frac{\partial\phi}{\partial x}=0 \quad (11)$$

where $x$ is the arbitrary outlet direction.

Symmetry axis:

Here the radial derivative of the variables is set to zero, i.e.:

$$\frac{\partial\phi}{\partial r}=0 \quad \text{and } V=0. \quad (12)$$

Solid–fluid interface:

The temperature at solid–gas interface is considered as the same, i.e.:

$$T_{w_{solid}}=T_{w_{gas}} \quad \text{and} \quad K_{solid}\frac{\partial T_{w_{solid}}}{\partial z}=K_{gas}\frac{\partial T_{w_{gas}}}{\partial z}.$$

### 2.3. Governing equation for the unsteady heat conduction

For the laser heated solid plate, the heat conduction in a stationary medium is considered in circumstances in which the temperature $T$ may vary with time $t$. Therefore, the equation yields a modified form of equation (3) with an addition of a laser heat source term. Thus:

$$\frac{\partial}{\partial t}(c_p\rho T)=\frac{\partial}{\partial x_i}\left[K\frac{\partial T}{\partial x_i}\right]+S. \quad (13)$$

It should be noted that $S$ is the unsteady spatially varying mathematical representation of the laser output power intensity distribution and is considered as

Gaussian with $1/e$ points equal to 0.375 mm i.e. the radius of the laser heated spot, from the centre of the beam. Thus:

$$S = \frac{I_0}{\sqrt{2\pi a}} \exp\left(-\frac{r^2}{a^2}\right) \delta \exp(-\delta \cdot z) f(t) \tag{14}$$

where $(I_0/\sqrt{2\pi a}) \exp[-(r^2/a^2)]$ is the intensity distribution across the surface, $\exp(-\delta \cdot z)$ is the absorption function and, $f(t)$ is the function which represents the time variation of the pulse shape.

Pulse heating:

The consecutive pulses consist of a series of same intensity pulses having the same pulse length (1.5 ms) but different cooling periods (repetition rates). The pulse lengths and intensities are given in Table 1. The repetitive pulse heating profile employed is not rectangular shape but have a rise and decay durations as shown in Fig. 1(b). The pulse rise and decay durations are kept constant for all the repetitive pulses for simplicity.

Boundary conditions for the governing energy equation in the solid:

Convection with a constant coefficient for still air is considered at the $z = 2$ mm thickness of boundary for the plate. At the interface continuity of temperature between the solid and the gas is enforced; far away from the laser source constant temperature $T = T_{amb}$ is assumed.

### 2.4. Variable properties

The density of air was considered to vary according to the ideal gas law depending on the local pressure and temperature while the specific heat capacity and thermal conductivity for both air and chromium steel were considered to be a function of temperature only. The dependence of properties on temperature and pressure are given in [16].

### 2.5. General form of the differential equations

The set of partial differential conservation equations governing the flow field are compactly represented by the following elliptic partial differential equation and the accompanying Table 2, which lists the dependent variables and the associated definitions of $\Gamma_\phi$ and $S_\phi$ [14].

$$\frac{\partial}{\partial t}(\rho\phi_j) + \frac{\partial}{\partial x_i}\left(\rho U_i \phi_j - \Gamma_\phi \frac{\partial \phi_j}{\partial x_i}\right) = S_{\phi_j}. \tag{15}$$

Table 1
Pulse properties for the three types of pulses used in the simulation

| Pulse type | Heating time (ms) | Cooling time (ms) | Repetition rate (pulses $s^{-1}$) | Peak power density (W $m^{-3}$) |
|---|---|---|---|---|
| 1 | 1.5 | 0.75 | 0.444 | $3 \times 10^{16}$ |
| 2 | 1.5 | 1.5 | 0.333 | $3 \times 10^{16}$ |
| 3 | 1.5 | 2.25 | 0.267 | $3 \times 10^{16}$ |

Table 2
Conservation equations corresponding to equation (15): $S = (I_0/\sqrt{2\pi a}) \exp[-(r^2/a^2)]\delta \exp(-\delta \cdot z) f(t)$ provided that $S$ is the external source term in the solid part. However, for details of the momentum source terms $S_{Mr,z}$, refer to Versteeg and Malalasekera [14]

| Conservation of | $\phi$ | $\Gamma_\phi$ | $S_\phi$ |
|---|---|---|---|
| Mass | 1 | 0 | 0 |
| Radial momentum | $V$ | $\mu_e$ | $-(\partial p/\partial r) + S_{Mr}$ |
| Axial momentum | $W$ | $\mu_e$ | $-(\partial p/\partial z) + S_{Mr}$ |
| Turbulent KE | $k$ | $\mu_e/\sigma_k$ | $G - \rho\varepsilon$ |
| Dissipation rate | $\varepsilon$ | $\mu_e/\sigma_e$ | $(\varepsilon/k)(C_1 G - C_2 \rho\varepsilon)$ |
| Thermal energy | $T$ | $\mu_e/\sigma_T$ | $\Phi + S$ |

## 3. Calculation of the field variables

### 3.1. The numerical technique

The particular practice that is chosen here for the derivation of the discretization equations is the Control Volume approach. The calculation domain is divided into subdomains or control volumes such that there is one control volume around a grid point. The differential equation is integrated over the control volume to yield the discretization equation. Thus, the discretization equation represents the same conservation principle over a finite region as the differential equation does over an infinitesimal region. The control-volume approach can be regraded as a special case of the method of weighted residuals, in which the weighting function is chosen to be unity over a control volume and zero everywhere else. The main reasons for choosing the control-volume formulation are its simplicity and easy physical interpretation. The formulation has also been shown, for a limited set of test problems, to be more accurate than the Galerkin method, which is a more popular weighted-residual technique [17]. The discretization process is not given here due to lengthy arguments, but refer to [14].

The grid used in the present calculations has $38 \times 70$ mesh points (Fig. 2), provided that the grid independent test is satisfied, which is shown in Fig. (3).

### 3.2. The calculation procedure for the flow field

If the pressure field which appears as a major part of the source term, for the momentum equations is known,

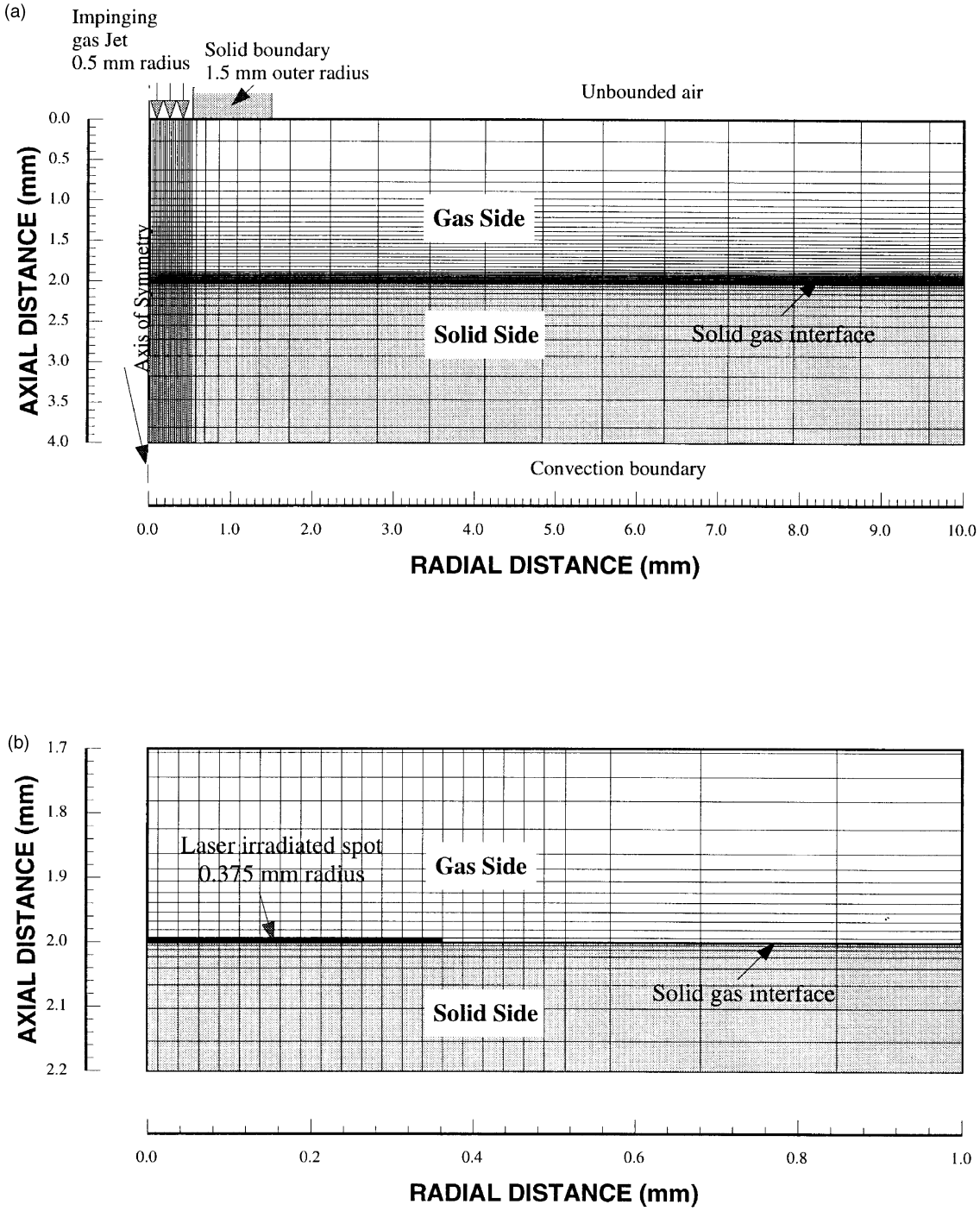


Fig. 2. View of the grid generated. (a) The solution domain with the computational grid. (b) A closeup view of the grid showing the laser irradiated spot.

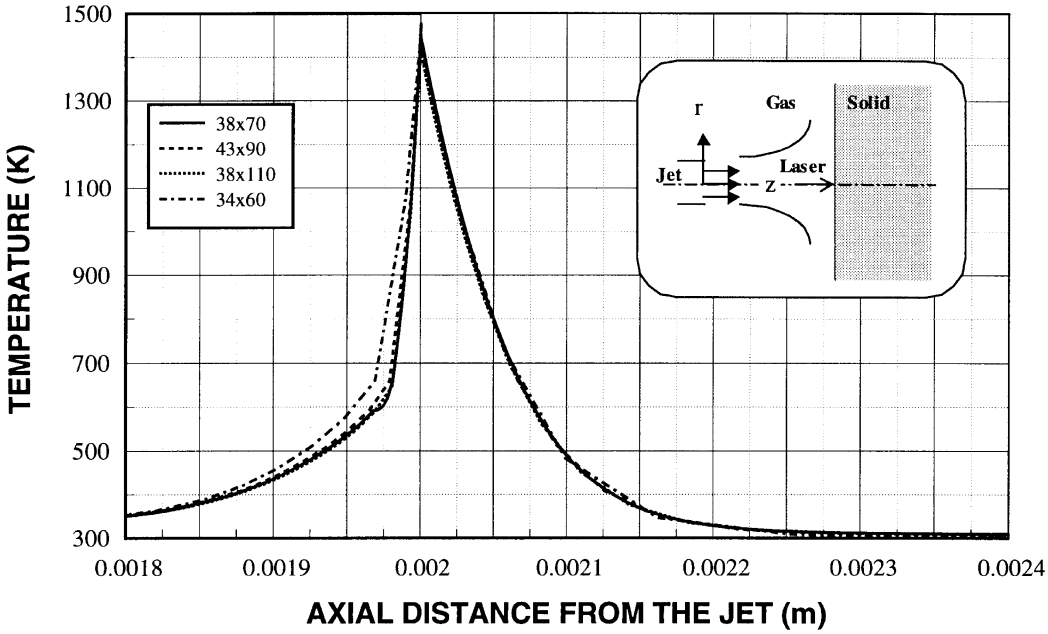


Fig. 3. The results of grid independence tests.

then the equation, which is written for each grid node, yields a closed set of algebraic equations, but there is no guarantee that the resultant velocity field would satisfy the continuity relation. The two problems of determining the pressure and satisfying continuity are overcome by adjusting the pressure field so as to satisfy continuity. A staggered grid arrangement is used in which the velocities are stored at a location midway between the grid points i.e. on the control volume faces. All other variables including pressure are calculated at the grid points. This arrangement gives a convenient way of handling the pressure linkages through the continuity equation and is known as the SIMPLE (Semi-Implicit Method for Pressure-Linked Equations) algorithm. This method is an iterative process to steady-state convergence. The details of this algorithm are found in [18].

### *3.3. The calculation procedure for heat conduction in the solid*

The governing equation for heat conduction in solid [equation (13)] can be written in the general equation (15) form. Thus the discretization procedure leads to algebraic equations of the form similar to flow equations with temperature $T$ replacing the general variable. No special calculation procedure is required to solve this equation since the energy equation is a stand alone independent equation. Although special care is taken to incorporate the spatially and time varying source, i.e. equation (14).

## 4. Validation of numerical simulations

To validate the numerical predictions, the previous experimental findings [19, 20] are used. In this case, a Reynolds number of 20 000 and a nozzle-to-plate spacing of two jet diameters are considered.

The present predictions and the experimental findings for a radial velocity ratio is shown in Fig. 4. The prediction agrees well with the experimental finding close to the stagnation region. As the radial distance ($r$) increases, small deviations between both results may be observed. This may be due to that the Lam–Bremhorst wall-damping functions which may slightly over predict the radial velocity developed away from the stagnation region.

Figure 5 shows the dimensionless mean velocity profiles with axial distance ($z$) for theoretical prediction and experimental finding. The low-Reynolds number $k$–$\varepsilon$ model prediction agrees well with the experimental finding. Therefore, the wall correction introduced in the low-Reynolds number $k$–$\varepsilon$ model well defines the mean velocity near the stagnation region.

When considering Figs 4 and 5, it may be observed that low-Reynolds number $k$–$\varepsilon$ model predictions agree considerably with the experimental findings in the stag-

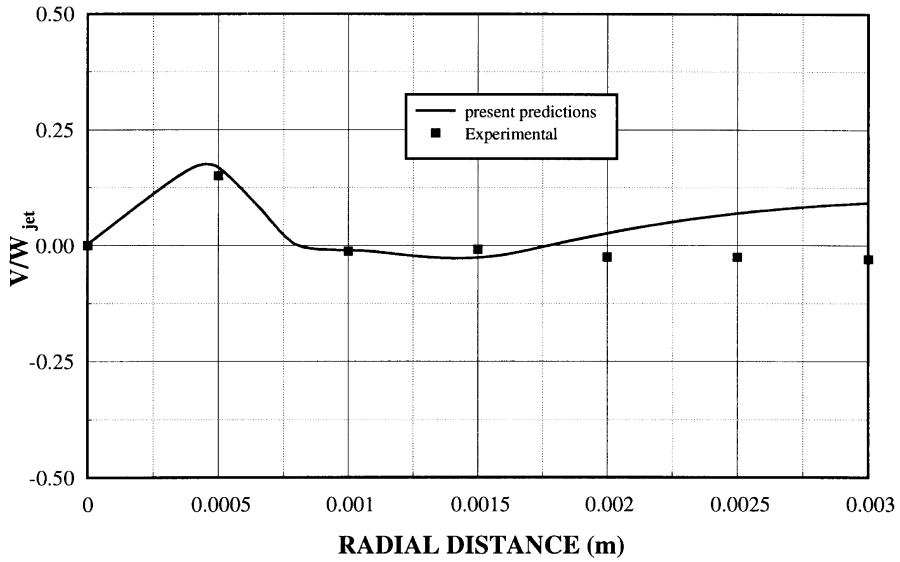


Fig. 4. Normalized radial velocity vs. radial distance. Experimental is Ashforth-First and Jamburnathran [20].

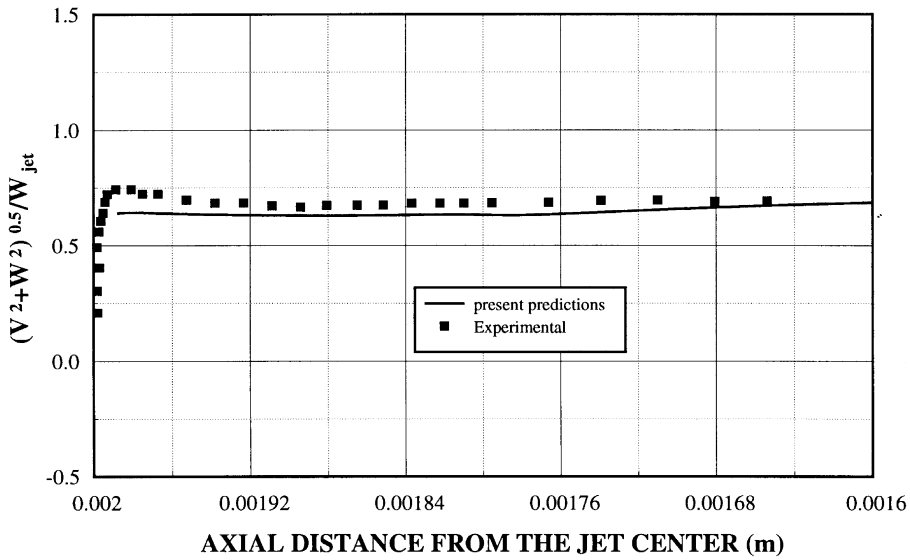


Fig. 5. Normalized mean velocity vs. axial distance. Experimental is Cooper et al. [19].

nation region. The laser spot size considered in the present study is almost within the stagnation region. Therefore, the discrepancies between the predictions and the experimental results in the far field of the flow have negligible effect on the laser induced heating process.

## 5. Results and discussions

The results obtained from the laser pulsative heating under the influence of assisting gas jet is presented as follows:

Figures 6 and 7 shows the temporal variation of surface and inside temperatures at different cooling periods for gas jet velocities of 10 m $s^{-1}$ and 100 m $s^{-1}$. The temperature profiles oscillate as the laser pulse repeats. The temperature builds up at the surface and inside the substance as the repetition rate increases (cooling period reduces), i.e. mean temperature profile shows an increasing trend at low cooling period. Almost identical temperature profiles resulted at a cooling period of 2.25 ms. However, the differences in peak to valley of temperature profiles appear to be considerable. Consequently, the

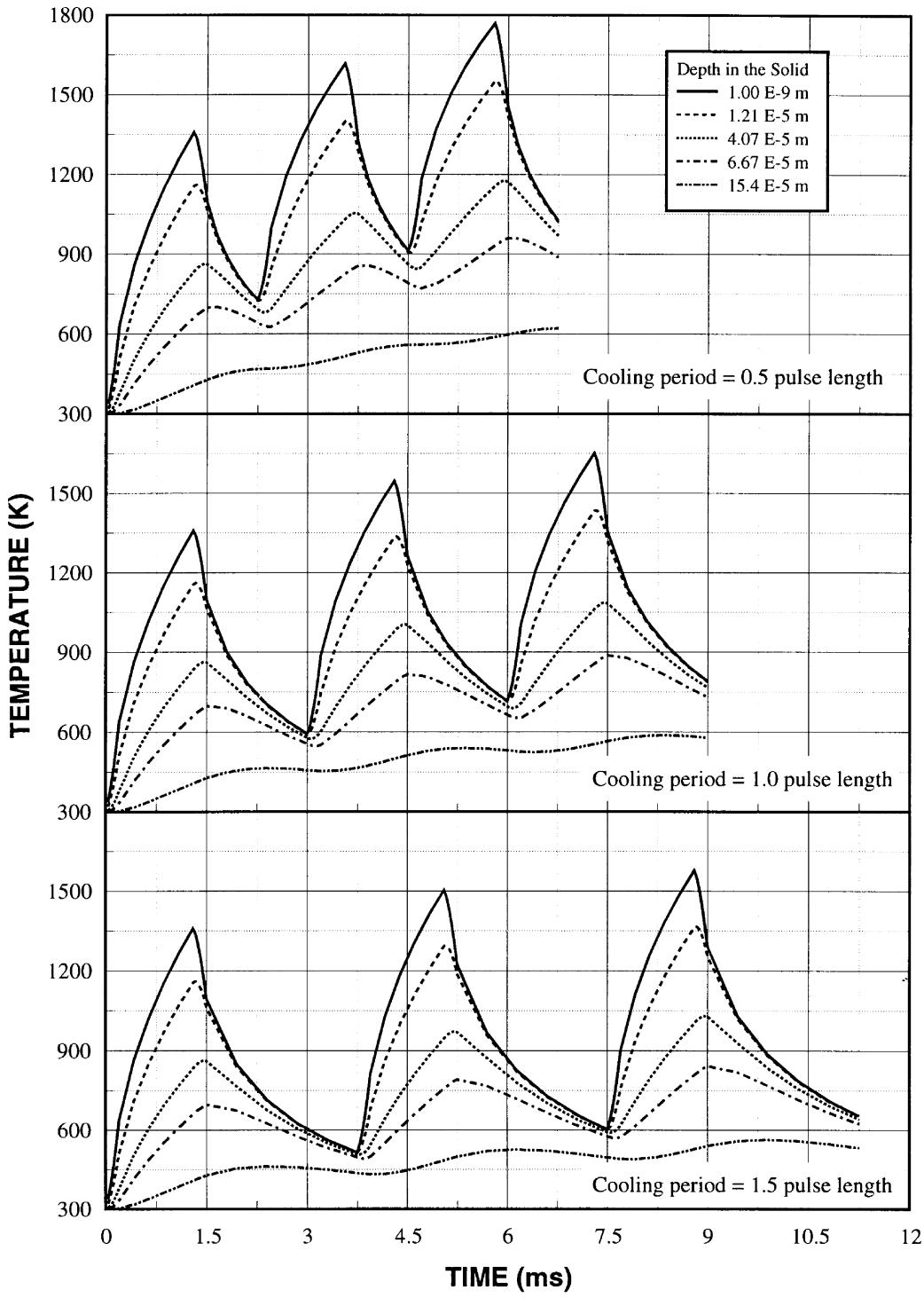


Fig. 6. Variation of temperature with time at various depths for the three types of pulses used in the simulation: radial location is 0.0125 mm from the centre of the jet and gas jet velocity is 10 m $s^{-1}$.

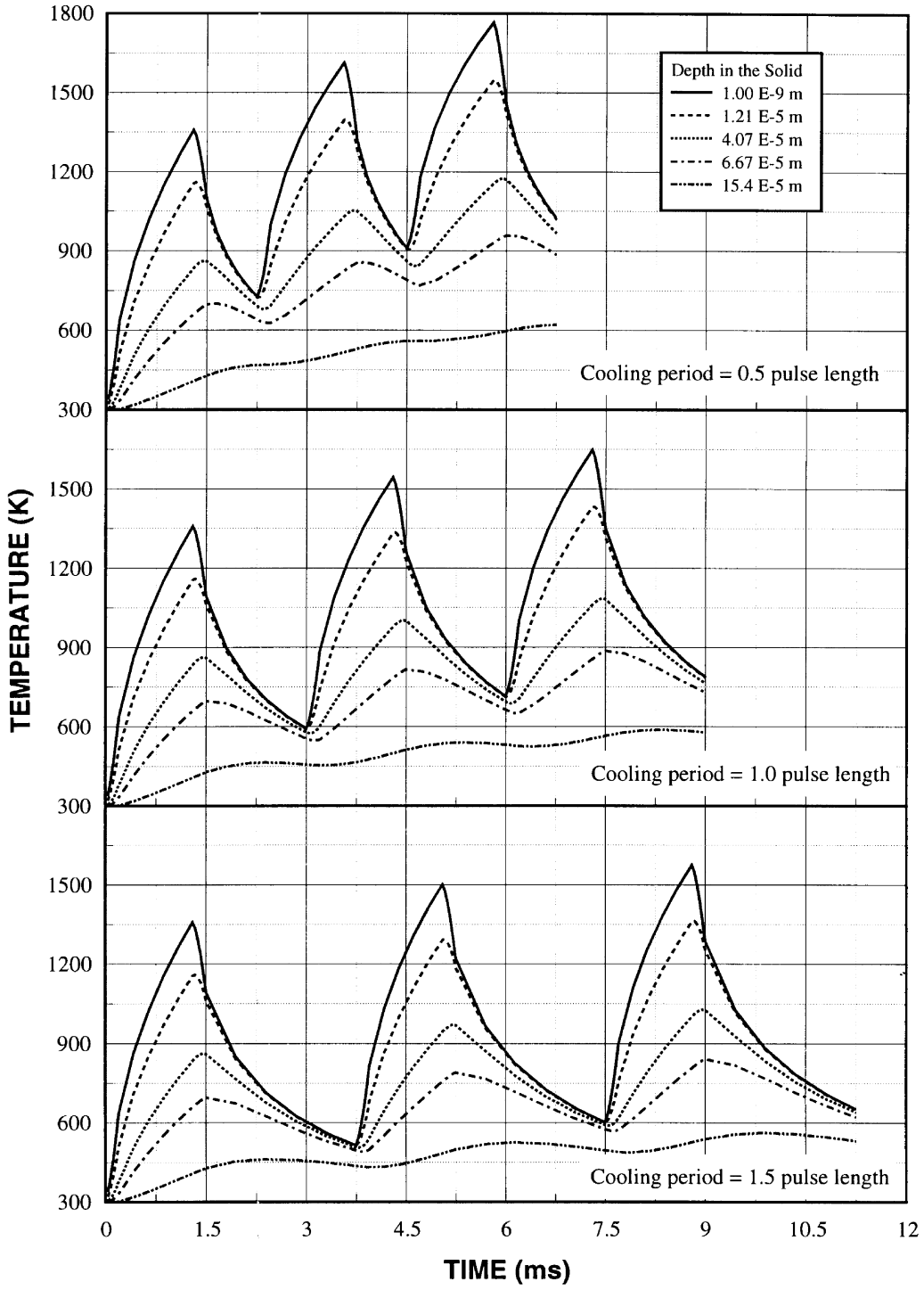


Fig. 7. Variation of temperature with time at various depths for the three types of pulses used in the simulation: radial location is 0.0125 mm from the centre of the jet and gas jet velocity is 100 m $s^{-1}$.

thermal integration appears to be impossible at the surface as well as at some depth below the surface. As the depth from the surface increases further, such as 0.154 mm, the temperature integration becomes visible at high cooling periods. In this case, the temperature profiles show either increasing trend or a small magnitude oscillation. The maximum value of temperature attained at this depth is of the order of 600 K, which may have a little influence on the metallurgical properties of the substance [21]. On the other hand, high amplitude oscillation in temperature in the surface vicinity may also result in high cycle thermal fatigue, which effects the mechanical and metallurgical properties of the substrate after the laser treatment. When comparing Figs 6 and 7, the influence of the gas jet velocity appear to be insignificant on the temperature profiles. This may be due to that the laser heated area is considerably small and the convection and diffusion processes which take place between the heated substrate surface and the gas jet are not substantiated due to the considerably low duration of pulsation.

Figures 8 and 9 shows the temporal variation of temperature profiles obtained at different depths in the solid and the radial location of 0.3625 mm from the irradiated spot centre for three pulse types and two gas jet velocities. Temperature profiles have an increasing trend for all the pulse types. The values of the temperature at these radial locations are considerably lower than those corresponding to irradiated spot centre. As the distance increases from the solid surface, the temperature attains lower values, and the temperature trend appears to be increasing for all the pulse types. In this case, even at certain depths below the surface the attainment of thermal equilibrium (isothermal heating) becomes unlikely. As indicated earlier the thermal integration at a depth below the irradiated spot centre is likely, but at some radial location at the same depth the thermal integration becomes unlikely. Consequently, overall view is that the thermal integration across the irradiated spot appears to be unlikely.

Figure 10 shows the temperature distribution in the axial direction at the consecutive pulse ends and at a radial location of 0.0125 mm away from the irradiated spot centre for three repetitive pulse types and 10 m/s gas jet velocity. The temperature in the solid rises considerably and the gap between the temperatures corresponding to heating and cooling cycles reduces as the cooling period reduces. The temperature decay is high after the completion of the first pulse, however, it reduces as consecutive pulses progress. This may indicate that the internal energy gain in the surface vicinity is considerably higher at the end of the first pulse and the temperature rises inside the solid substance as the pulse repetition progresses due to conduction. On the other hand, as the cooling period increases, the temperature gradient in the solid after the consecutive pulses becomes almost the same as that resulted from the first pulse. In addition, the gap between the temperatures due to heating and cooling cycles reduces. The peak to valley temperature difference is very high; in this case, the thermal integration inside the solid substrate is less likely for this particular cooling period. The temperature decay in the gas side close to solid surface appears to be almost linear provided that higher the surface temperature results in higher the temperature gradient in the surface region. In the case of a cooling cycle, temperature gradient in the gas side is low. This indicates that the gas in the surface vicinity is not effected significantly from the heat diffusion generated due to the previously heated surface, i.e. a high pressure region is developed in this region, which in turn results in radial flow, therefore, convective cooling of the surface accelerates and the heated gas is swept away.

Figure 11 shows the axial temperature distribution at the pulse ends and a radial position of 0.3625 mm away from the irradiated spot centre for three repetitive pulse types and 10 m $s^{-1}$ gas jet velocity. In the heating cycle, the temperature increases slightly as the cooling period between the pulses decreases. The gap between the temperature is almost the same for all the pulse types. In addition, the gap between the temperatures resulted due to heating and cooling cycles is not considerable. Therefore, the thermal integration in this region becomes likely i.e. the pulse types have no significant influence on the resulting temperature profiles. In the gas side the temperature somewhere beyond the surface vicinity reaches maximum value and becomes higher than the surface temperature. This may be due to one or all of the following facts: (i) In the surface vicinity radial flow developed sweeps the heated gas away in this region at a faster rate than the neighboring region, and (ii) the heated gas which has been swept away from the irradiated spot centre may mix with the impinging gas in the boundary layer next to the surface vicinity. Therefore, the heat accumulated in this region may not be diffused at a fast rate, which in turn results in the temperature rise in this region. This argument is true for all the pulse types employed. In addition, the temperature decays rapidly as the axial distance increases further away from the surface. In this case low temperature gas jet purges the hot gas further downstream in the radial direction.

Figure 12 shows the temperature variation in the axial direction at a radial location of 0.0125 mm from the irradiated spot centre and at the pulse ends of three pulse types for 100 m $s^{-1}$ gas jet velocity. The temperature profiles developed in the solid substrate is almost the same as those obtained for 10 m $s^{-1}$. Consequently, the effect of gas jet velocity on the resulting temperature profiles is not considerable. Temperature decays more faster than that occurs for 10 m $s^{-1}$ gas jet velocity. In this case, the pressure developed in the stagnation region rises considerably, which in turn further accelerates the radial flow. In addition, high velocity gas jet suppresses

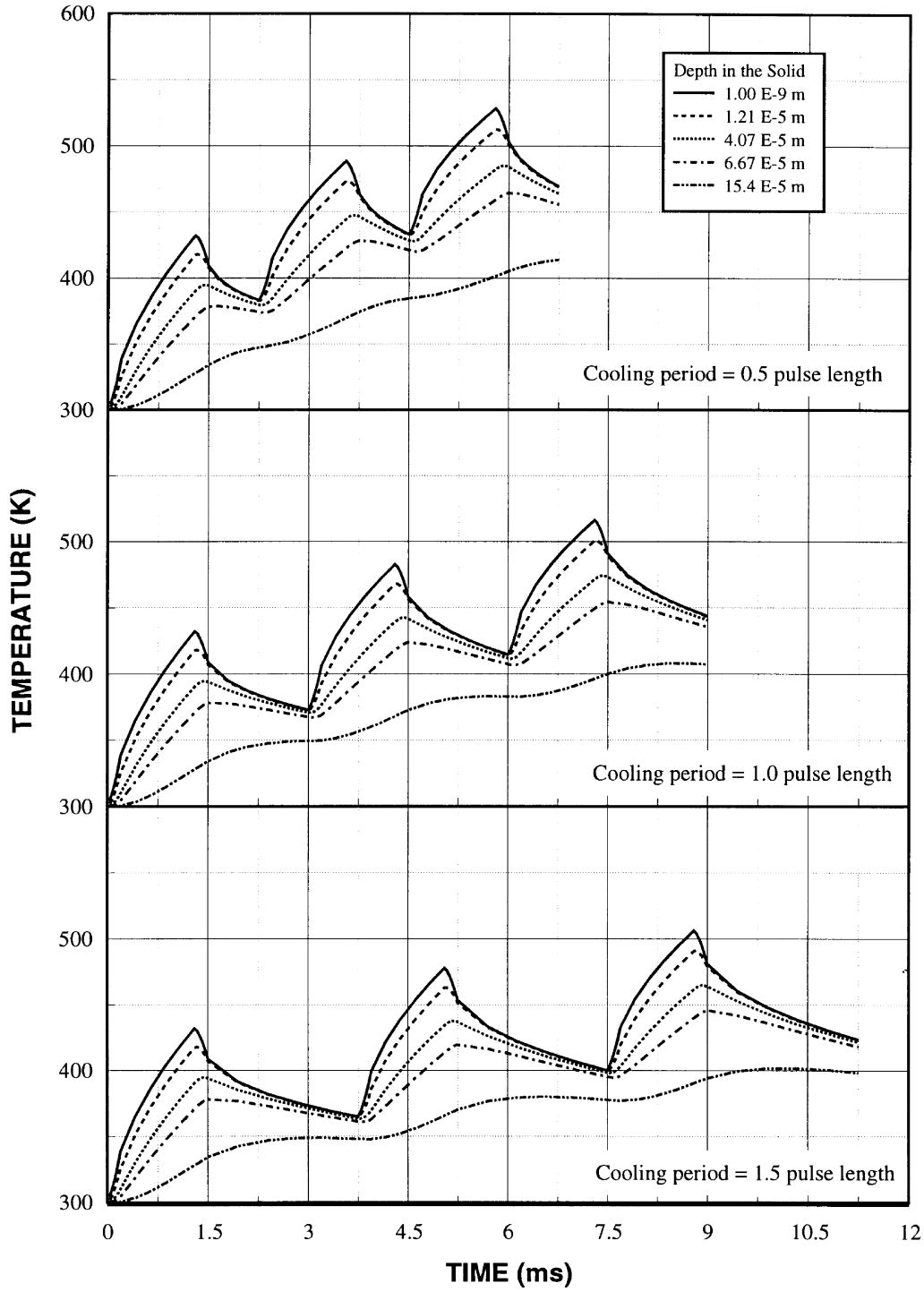


Fig. 8. Variation of temperature with time at various depths for the three types of pulses used in the simulation: radial location is 0.3625 mm from the centre of the jet and gas jet velocity is 10 m $s^{-1}$.

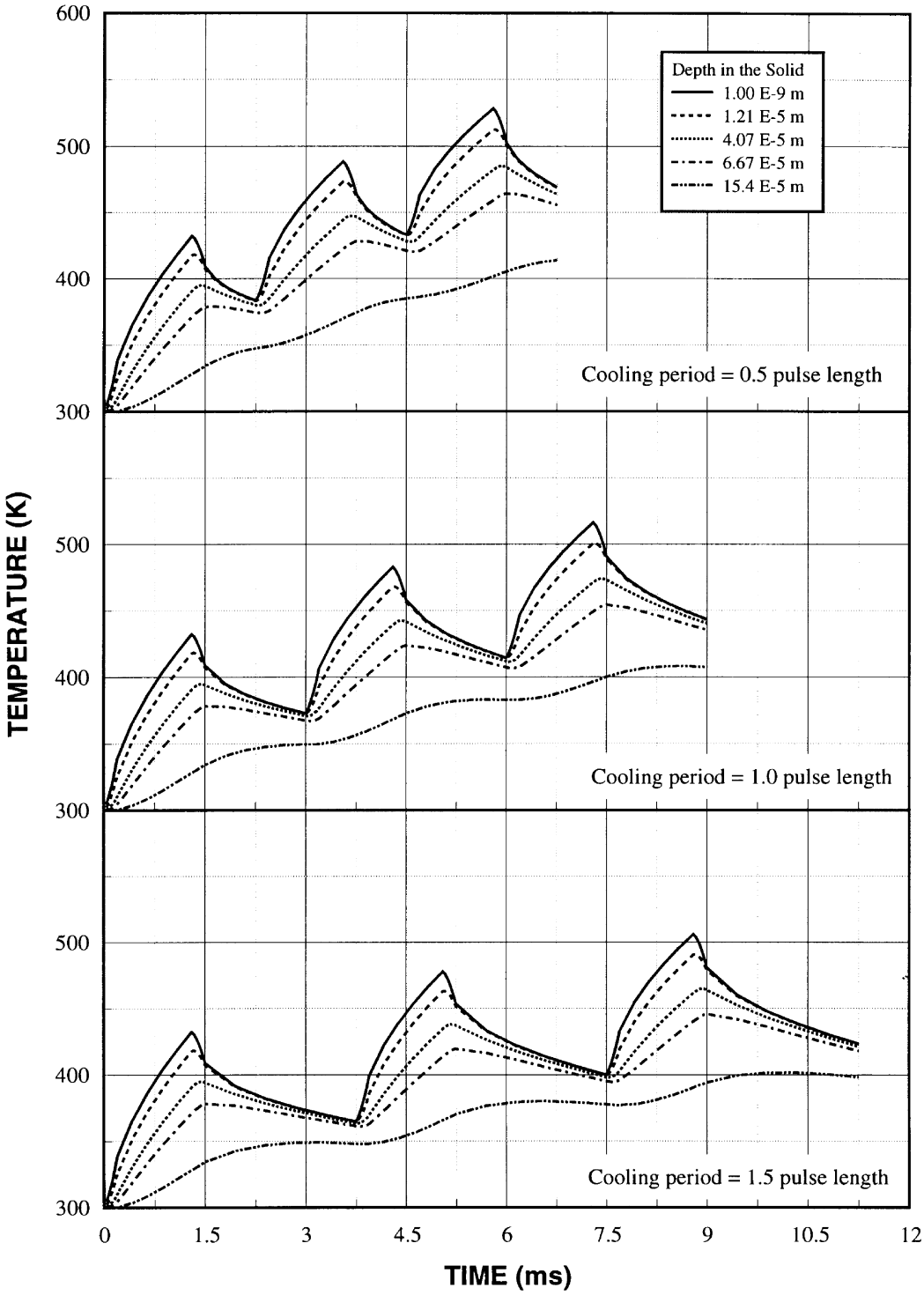


Fig. 9. Variation of temperature with time at various depths for the three types of pulses used in the simulation: radial location is 0.3625 mm from the centre of the jet and gas jet velocity is 100 m $s^{-1}$.

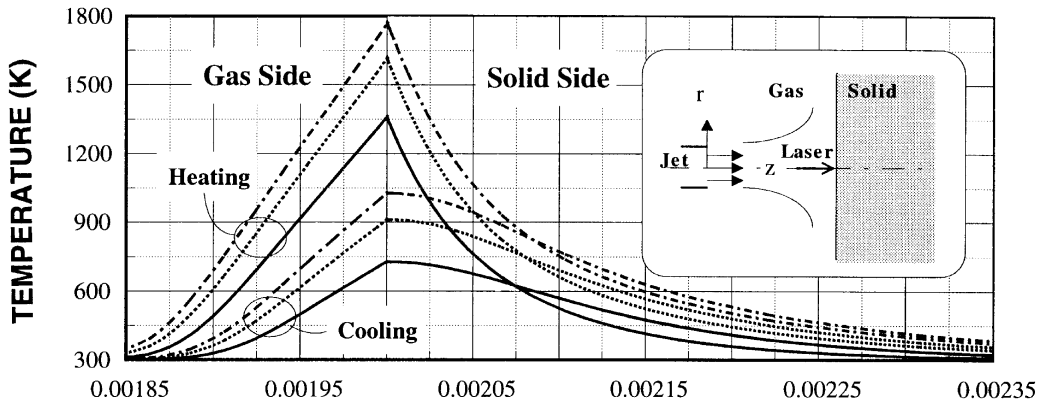


(a) pulse type 1 (cooling period = 0.5 pulse length)

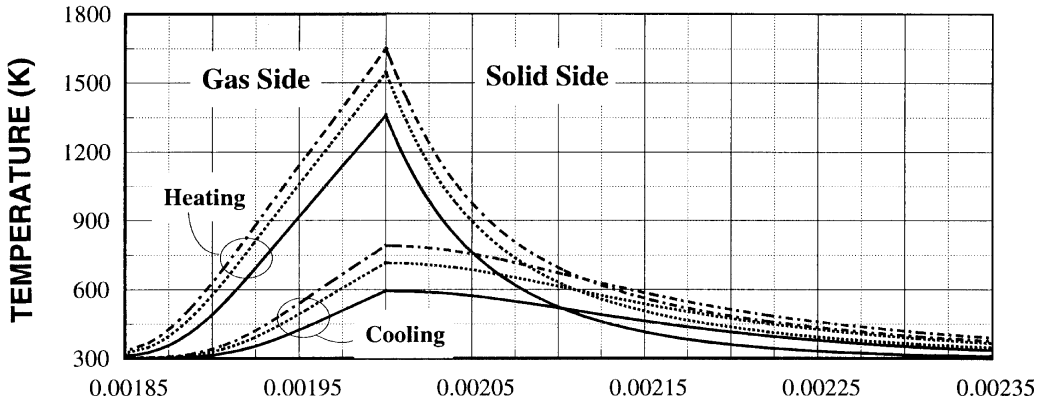


(b) pulse type 2 (cooling period = 1.0 pulse length)

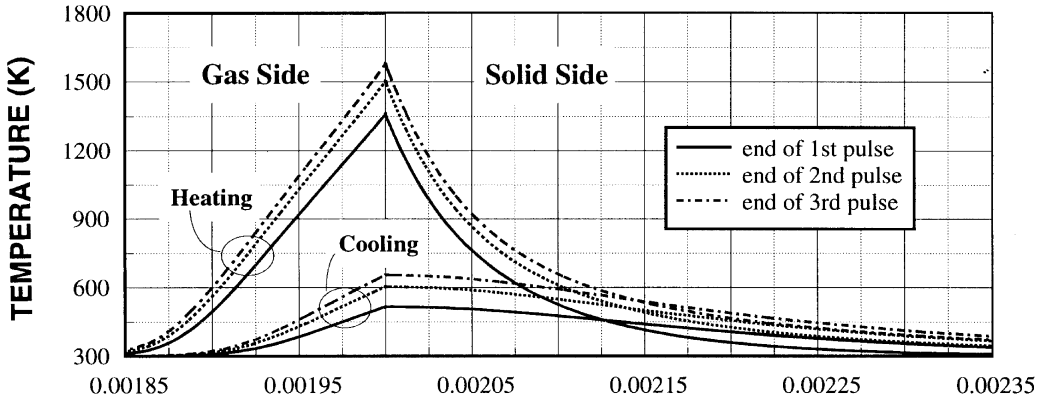


(c) pulse type 3 (cooling period = 1.5 pulse length)

Fig. 10. Temperature profiles in the axial direction obtained at the end of heating and cooling periods for the three types of pulses used; the radial location is 0.0125 mm from the centre of irradiated spot and gas jet velocity is 10 m $s^{-1}$. (a) Pulse type 1 (cooling period = 0.5 pulse length). (b) Pulse type 2 (cooling period = 1.0 pulse length). (c) Pulse type 3 (cooling period = 1.5 pulse length).

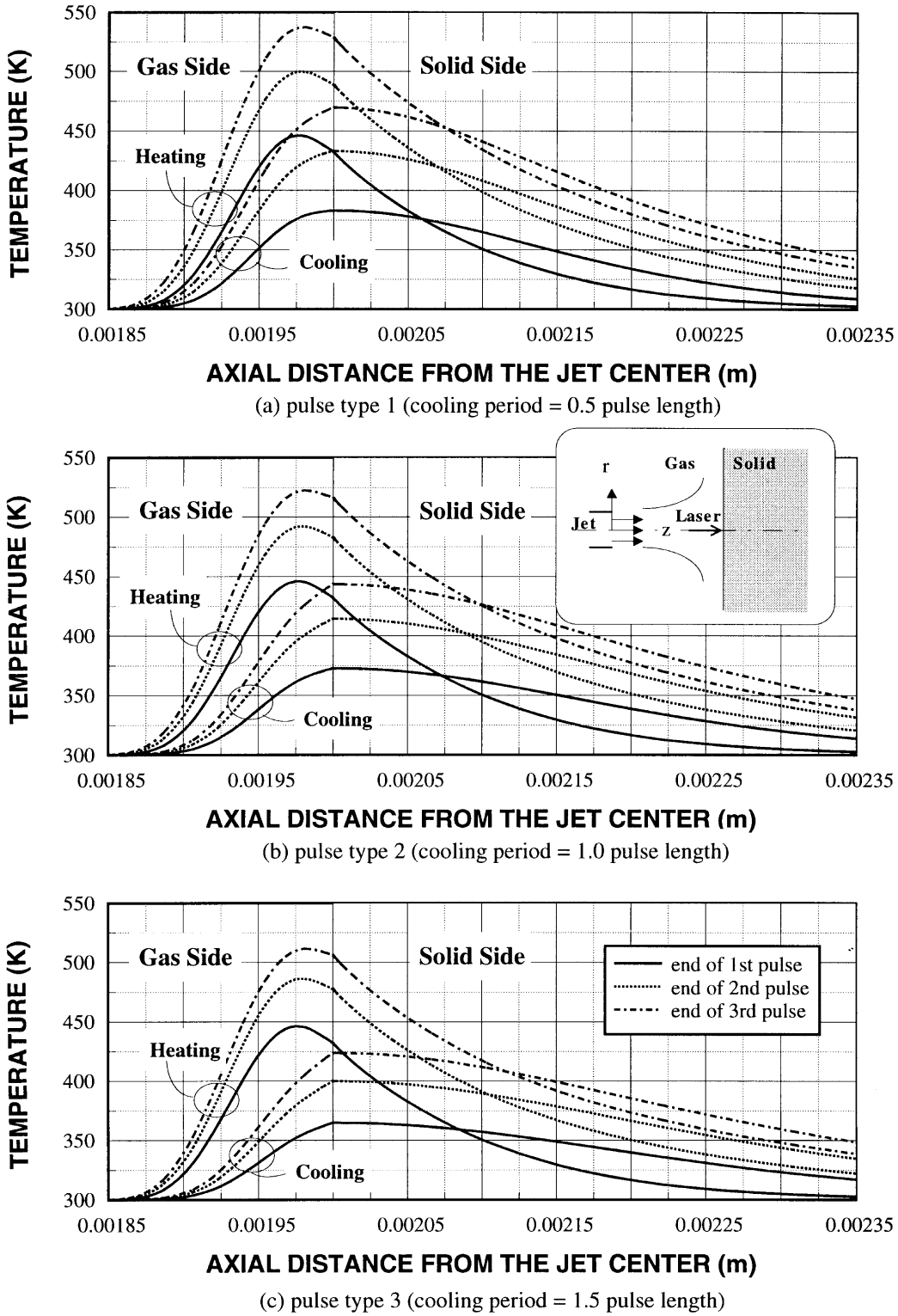


Fig. 11. Temperature profiles in the axial direction obtained at the end of heating and cooling periods for the three types of pulses used; the radial location is 0.3625 mm from the centre of irradiated spot and gas jet velocity is 10 m $s^{-1}$. (a) Pulse type 1 (cooling period = 0.5 pulse length). (b) Pulse type 2 (cooling period = 1.0 pulse length). (c) Pulse type 3 (cooling period = 1.5 pulse length).

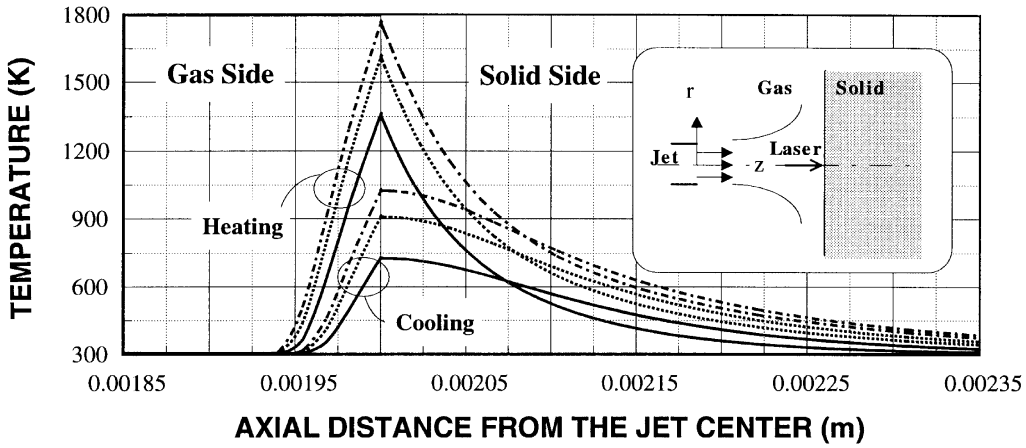


(a) pulse type 1 (cooling period = 0.5 pulse length)

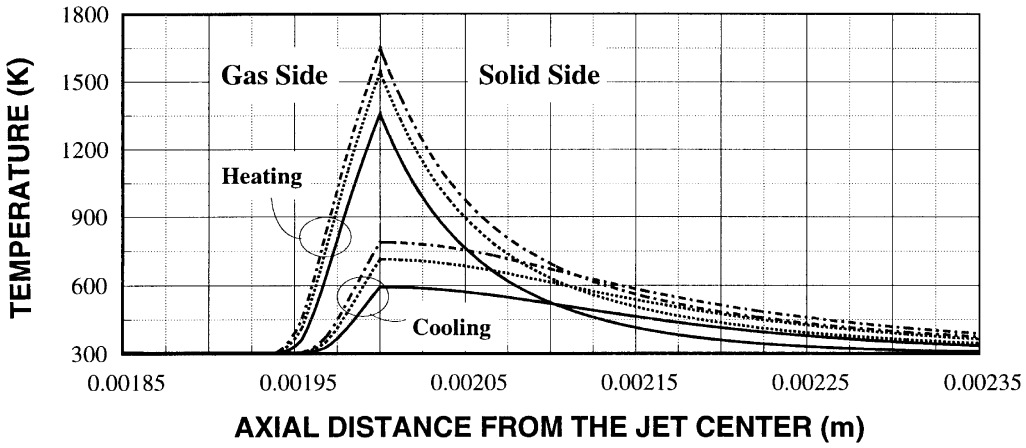


(b) pulse type 2 (cooling period = 1.0 pulse length)

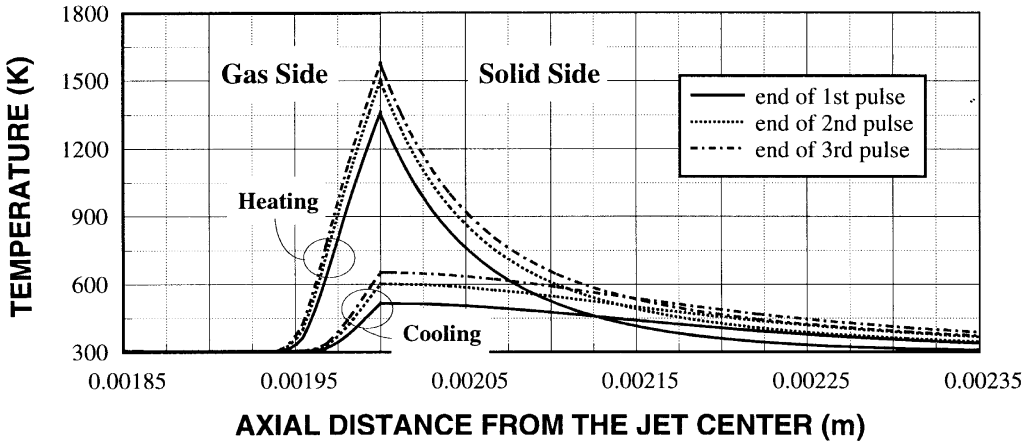


(c) pulse type 3 (cooling period = 1.5 pulse length)

Fig. 12. Temperature profiles in the axial direction obtained at the end of heating and cooling periods for the three types of pulses used; the radial location is 0.0125 mm from the centre of irradiated spot and gas jet velocity is 100 m $s^{-1}$. (a) Pulse type 1 (cooling period = 0.5 pulse length). (b) Pulse type 2 (cooling period = 1.0 pulse length). (c) Pulse type 3 (cooling period = 1.5 pulse length).

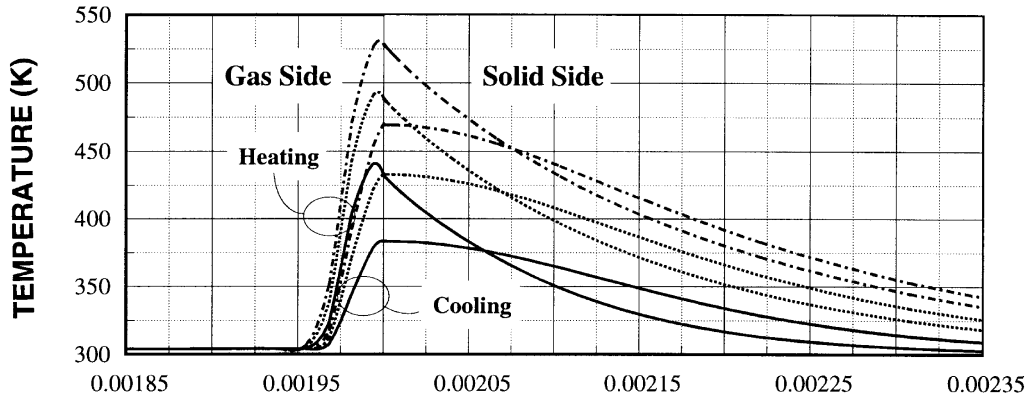


(a) pulse type 1 (cooling period = 0.5 pulse length)

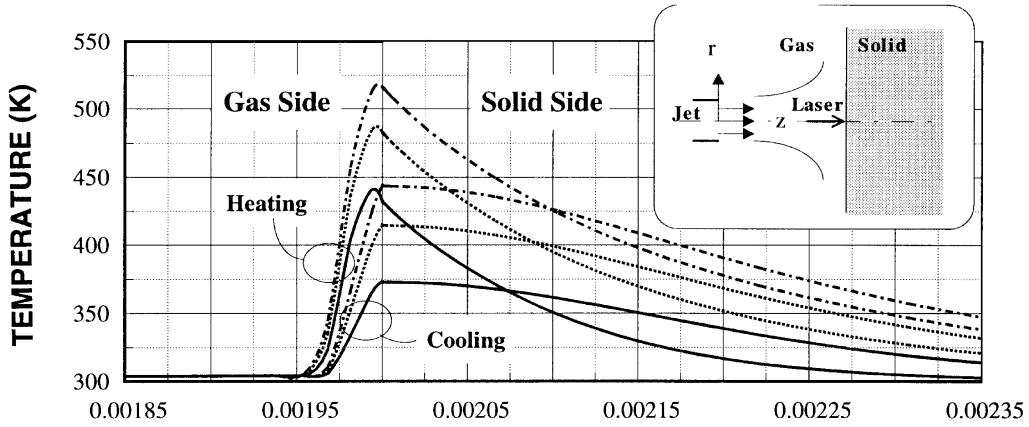


(b) pulse type 2 (cooling period = 1.0 pulse length)

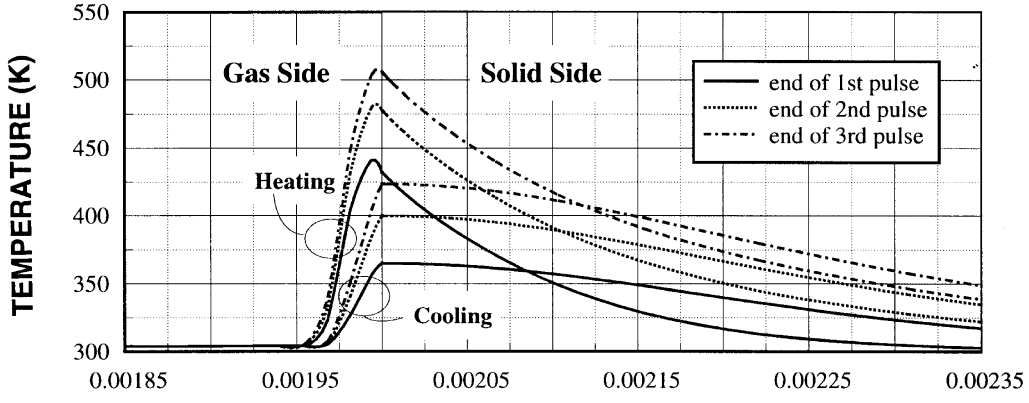


(c) pulse type 3 (cooling period = 1.5 pulse length)

Fig. 13. Temperature profiles in the axial direction obtained at the end of heating and cooling periods for the three types of pulses used; the radial location is 0.3625 mm from the centre of irradiated spot and gas jet velocity is 100 m $s^{-1}$. (a) Pulse type 1 (cooling period = 0.5 pulse length). (b) Pulse type 2 (cooling period = 1.0 pulse length). (c) Pulse type 3 (cooling period = 1.5 pulse length).

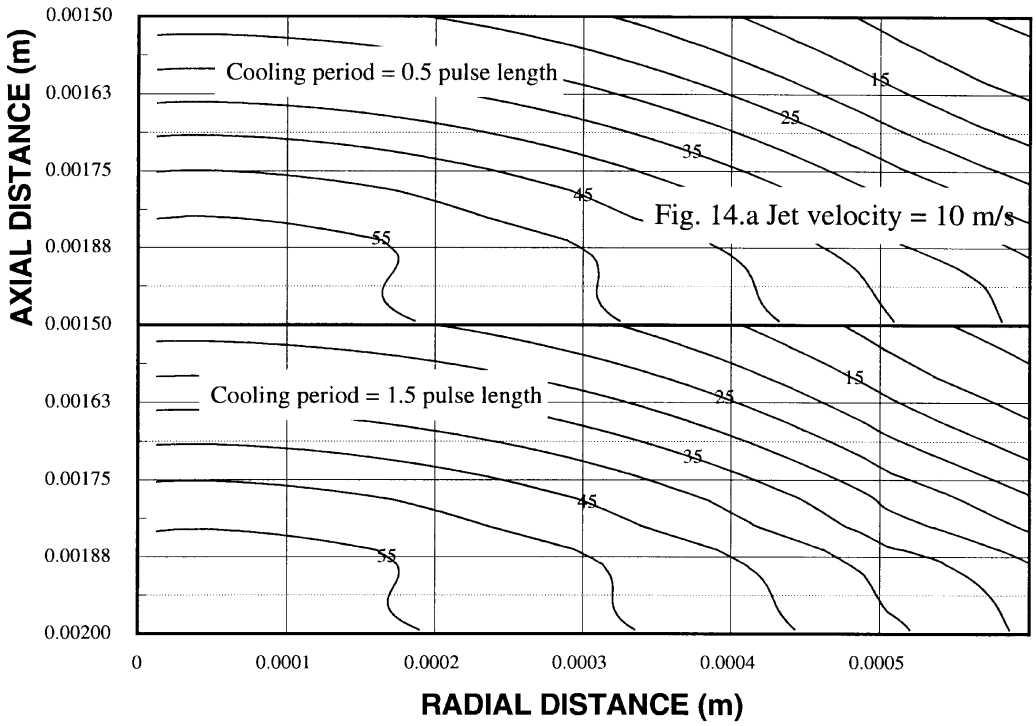


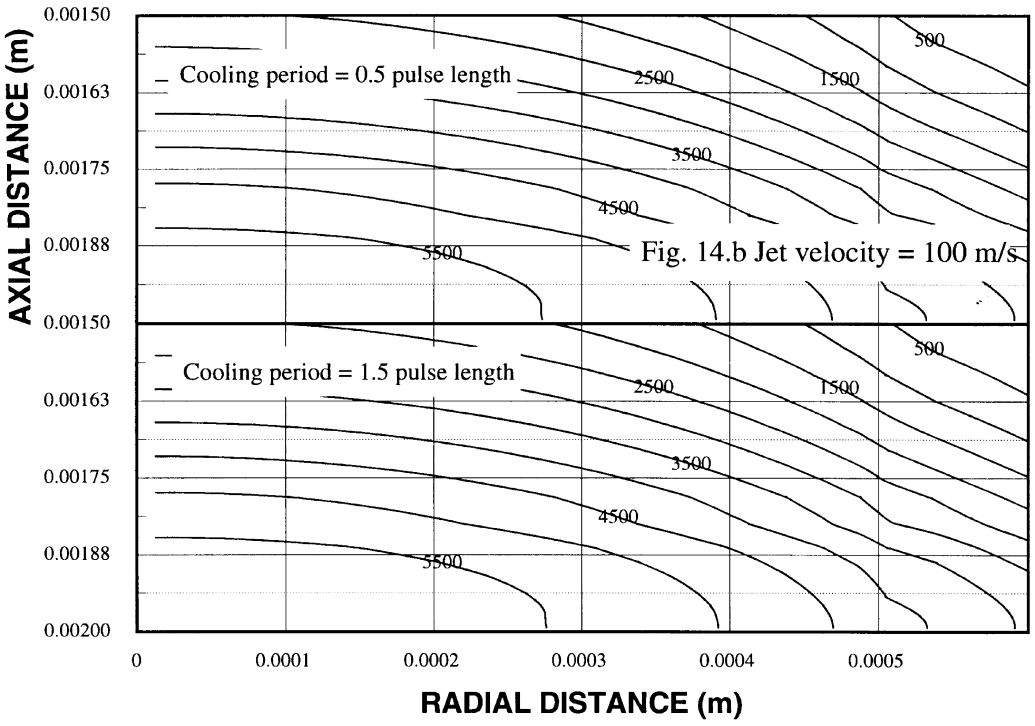


Fig. 14. Pressure contours obtained for two different types of pulses used in the simulation and gas jet velocities of 10 and 100 m $s^{-1}$.

the stagnation region further close to the solid surface, therefore, next to the surface vicinity the cool gas jet dominates, resulting in low temperature attainment in this region.

Figure 13 shows the axial temperature distribution at the end of the pulses and a radial location of 0.3625 mm away from the irradiated spot centre for three pulse types and 100 m $s^{-1}$ gas jet velocity. The temperature profiles in the solid side appear to be similar to those obtained for 10 m $s^{-1}$ gas jet velocity. In the gas side, temperature profiles in the axial direction decays at a considerably fast rate. This may again be due to the development of the radial flow.

Figure 14 shows the radial pressure distribution for two gas jet velocities and two cooling period ratios. The radial pressure gradually builds towards the workpiece surface for 10 m $s^{-1}$ gas jet velocity and the pressure variation in the radial direction is not substantiated, which in turn results in the low radial velocity attainment in this region. The influence of cooling period on the radial pressure contours is not significant. Alternatively, when comparing Figs 14a and b, the radial pressure variation for 100 m $s^{-1}$ gas jet velocity is considerable; in this case, the radial flow due to pressure difference is substantial.

## 6. Conclusions

The conclusions derived from the present study may be listed as follows:

(1) The repetitive pulse with low cooling period results in increasing rate of peak to valley temperature difference. In this case, the temperature integration inside and at the surface of the workpiece is unlikely. However, for the repetitive pulses having long cooling period results in identical temperature profiles being developed at the surface and inside the solid material, and, the peak to valley temperature difference is considerable.

(2) As the radial distance increases from the irradiated spot centre, the amplitude of the temperature oscillation reduces. This may be due to the spatial power intensity distribution, of the laser beam, which is considered as Gaussian.

(3) The amplitude of the temperature distribution decreases considerably as the distance from the surface increases. This is especially true for the repetitive pulses with moderate cooling period. In this case, the thermal integration may become likely. However, none of any of the repetitive pulse types used in the present study results in thermal integration at the workpiece surface.

(4) The gas side temperature also oscillates similar to that occurs at the solid surface. As the radial distance increases the gas side temperature at some distance away from the surface attains high values. This may be due to radial flow of the fluid in the surface vicinity, which in turn accelerates the mixing of the heated gas in the surface vicinity with the impinging gas jet.

(5) The impinging gas jet velocity has almost no effect on the solid side temperatures. However, it has a great influence on the development of the gas side temperature. In this case, rapid decay of the gas side temperature occurs in the surface vicinity for high gas jet velocity.

(6) The influence of cooling period ratio on the resulting velocity and pressure fields is negligible. Therefore, the flow thermal properties may not be effected by the heat transfer from the irradiated spot. In addition, the radial flow is substantiated, due to the high radial pressure gradient attainment, for high gas jet velocity.

## Acknowledgement

The authors acknowledge the support of King Fahd University of Petroleum and Minerals, Dhahran, Saudi Arabia for this work.

## References

[1] Schultz W, Becker D, Franke J, Kemmerling R, Herziger G. Heat conduction losses in laser cutting of metals. Journal of Physics D, Trans Applied Physics 1993;26:1357–63.

[2] Rappaz M, Hoadley AFA, Zimmermann M. Heat flow simulation of laser remelting with experimental validation. Metallurgical Transactions B 1991;22B:101–9.

[3] Yilbas BS. A study into $CO_2$ laser cutting process. Heat and Mass Transfer 1997;32:175–80, 1997.

[4] Osawa M, Yoneyama T, Isskiki Y. Effect of laser treatment on inter granular corrosion of austenitic stainless steel. Corrosion Engineering 1995;44(3):159–65.

[5] Toyol M, Mukherjee K. Thermal and microstructural analysis for laser surface hardening of steel. Journal of Applied Physics 1994;75(8):3855–61.

[6] Yilbas BS, Sahin A. Laser heating mechanism including evaporation process initiating laser drilling. International Journal of Machine Tools and Manufacturing 1995;35:1047–62.

[7] Sun Y, Weng C, Tei-Chen C, Li W. Estimation of surface absorptivity and surface temperature in laser surface hardening process. Japanese Journal of Applied Physics 1996;35(6A):3658–64.

[8] Ariel PD. Stagnation point flow—a free boundary value problem formulation. International Journal of Computer Mathematics 1993;49(1–2):123–31.

[9] Amin N, Riley N. Free convection at an axisymmetric

stagnation point. Journal of Fluid Mechanics 1996;314:105–12.
[10] Baukal CE, Gebhart B. A review of semi-analytical solutions for flame impingement. International Journal of Heat and Mass Transfer 1996;39(4):2989–3002.
[11] Abid R, Speziale CG. The freestream matching condition for stagnation point turbulent flows: an alternative formulation. Journal of Applied Mechanics 1996;63:95–100.
[12] Strahle WC. Stagnation point flows with freestream turbulence—the matching condition. AIAA Journal 1985;23:1822–4.
[13] Rodi W. Turbulence models and their application in hydraulics—a state of the art review. International Association for Hydraulic Research, University of Karlsruhe, Karlsruhe, 2nd ed., 1984.
[14] Versteeg HK, Malalasekera W. An Introduction to Computational Fluid Dynamics, The Finite Volume Method. Longman Scientific and Technical, 1995.
[15] Elkaim D, Reggio M, Camarero R. Simulating two-dimensional turbulent flow by using the $k$–$\varepsilon$ model and the vorticity–streamfunction formulation. International Journal for Numerical Methods in Fluids 1992;14:961–80.
[16] Incropera FP, Dewitt DP. Introduction to Heat Transfer. John Wiley and Sons, 1985. pp. 667–96, Appendix A.
[17] Patankar SV. Computer Analysis of Fluid Flow and Heat Transfer, Chap. 8. Swansea, U.K.: Pineridge Press Ltd, 1981. pp. 223–52.
[18] Patankar SV. Numerical Heat Transfer. New York: McGraw-Hill, 1980.
[19] Cooper D, Jackson DC, Launder BE, Liao GX. Impinging jet studies for turbulence model assessment—I. Flow-field experiments. International Journal of Heat and Mass Transfer 1993;36(36):2675–84.
[20] Ashforth-First S, Jamburnathran P. Numerical prediction of semi-confined jet impingement and comparisons with experimental data. International Journal for Numerical Methods in Fluids 1996;23:295–306.
[21] Duley WW. Laser Processing and Analysis of Materials. New York: Plenum Press, 1983.